ENVIRONMENTAL STUDIES

Subglacial discharge accelerates future retreat of Denman and Scott Glaciers, East Antarctica

Tyler Pelle[1]*, Jamin S. Greenbaum[1], Christine F. Dow[2], Adrian Jenkins[3], Mathieu Morlighem[4]

Ice shelf basal melting is the primary mechanism driving mass loss from the Antarctic Ice Sheet, yet it is unknown how the localized melt enhancement from subglacial discharge will affect future Antarctic glacial retreat. We develop a parameterization of ice shelf basal melt that accounts for both ocean and subglacial discharge forcing and apply it in future projections of Denman and Scott Glaciers, East Antarctica, through 2300. In forward simulations, subglacial discharge accelerates the onset of retreat of these systems into the deepest continental trench on Earth by 25 years. During this retreat, Denman Glacier alone contributes 0.33 millimeters per year to global sea level rise, comparable to half of the contemporary sea level contribution of the entire Antarctic Ice Sheet. Our results stress the importance of resolving complex interactions between the ice, ocean, and subglacial environments in future Antarctic Ice Sheet projections.

INTRODUCTION

Ice shelf basal melting, driven primarily by warm ocean currents upwelling along the base of Antarctic ice shelves (1, 2), comprises over half of the contemporary mass loss of Antarctica's ice shelves and drives accelerated ice flow that promotes upstream glacial thinning (3–6). This ocean-induced melting has driven rapid thinning of glaciers along the Amundsen Sea Embayment of West Antarctica, where ocean temperatures adjacent to Pine Island and Thwaites Glaciers exceed 1°C (7–9). Upstream thinning has also been observed (10, 11) along coastal sectors of the East Antarctic Ice Sheet, which has long been considered the stable counterpart of West Antarctica because of both its topographic configuration and the relatively cold ocean waters that occupy the continental shelf. However, a recent satellite-based circum-Antarctic assessment (12) of ice shelf basal melt highlighted that the maximum melt rate inferred across all Antarctic ice shelves between 2010 and 2018 occurred ~10 km downstream of Denman Glacier (126 ± 3 m/year), East Antarctica, where observed (13) on-shelf ocean temperatures average −1.26 ± 0.04°C (Fig. 1A). In contrast, melt rates of the Scott Ice Tongue, located adjacent to Denman Glacier, peak at 19 ± 1 m/year under similar ocean conditions. As contemporary ice sheet models compute basal melt rates as functions of sub–ice shelf ocean temperatures and basal geometries (14–16), the higher melt rates experienced by the Denman Ice Tongue relative to that of West Antarctic ice shelves and the Scott Ice Tongue cannot be reconciled by the available generation of ice shelf melt models. That is, unless ocean temperature observations near the terminus of Denman Glacier are underestimated by 2°C, there must be other processes driving elevated rates of basal melting within this glacier's grounding zone. In this study, we will investigate the uncharacteristically high ice shelf melt rates that force Denman Glacier.

Denman Glacier, located along the Queen Mary Coast of East Antarctica, contains 1.5 m of global sea level potential in ice grounded below sea level (17) and has been experiencing upstream thinning of 0.4 ± 0.1 m/year (18), acceleration of 17 ± 4% (19), and mass loss equivalent to 10% of its yearly volume flux since the late 1970s (10). Furthermore, Denman Glacier's grounding line (i.e., the downstream limit of where ice remains in contact with the underlying bedrock) has retreated 5.4 ± 0.3 km between 1996 and 2018 (18) back toward the deepest (3.5 km below sea level) (17) continental trench on Earth (Fig. 1). As this trench is located along Denman Glacier's ice stream, we hypothesize that this topographic setting is optimal to channelize the subglacial water system close to the grounding line, which outflows into the sub–ice shelf ocean cavity and locally enhances basal melt rates. This process has been extensively studied in application to Arctic glaciers (20–24); however, its application to Antarctic glaciers is limited to indirect inference (25–27) and the correspondence of locations of modeled subglacial discharge and basal melt maxima (28–30) because of inaccessibility of Antarctic grounding lines and sub–ice shelf ocean cavities. The potential of this melt enhancement process to be a prominent forcing mechanism of future retreat of Antarctic outlet glaciers has yet to be assessed in a realistic numerical ice sheet modeling framework and thus represents a major knowledge gap in modern-day glaciology.

To address this, we build from previous plume-modeling results (14, 32) to develop a parameterization of ice shelf basal melt that accounts for ocean and subglacial discharge forcing (See Materials and Methods). We then apply this parameterization in future ice sheet model simulations of Denman and Scott Glaciers using the Ice-sheet and Sea-level System Model (ISSM) (33) to examine their potential dynamic evolutions through 2300. We perform three ocean-forced simulations under Shared Socioeconomic Pathways (SSP) emission scenarios defined by the Intergovernmental Panel on Climate Change: (i) Ocean forcing between 1992 and 2017 is repeated through 2300 (CTRL), (ii) low emission (SSP1-2.6), and (iii) high emission (SSP5-8.5 with extrapolated warming of 2°C from 2100 to 2300). For each scenario, we compute melt with and without including the present-day subglacial discharge flux field (e.g., SSP5-8.5$_{SD}$ in Fig. 2) to discern the relative impacts that ocean and discharge conditions have on the future

[1]Scripps Institution of Oceanography, University of California, San Diego, La Jolla, CA, USA. [2]Department of Geography and Environmental Management, University of Waterloo, Waterloo, ON, Canada. [3]Department of Geography and Environmental Sciences, Northumbria University, Newcastle upon Tyne, NE1 8ST, UK. [4]Department of Earth Sciences, Dartmouth College, Hanover, NH, USA.
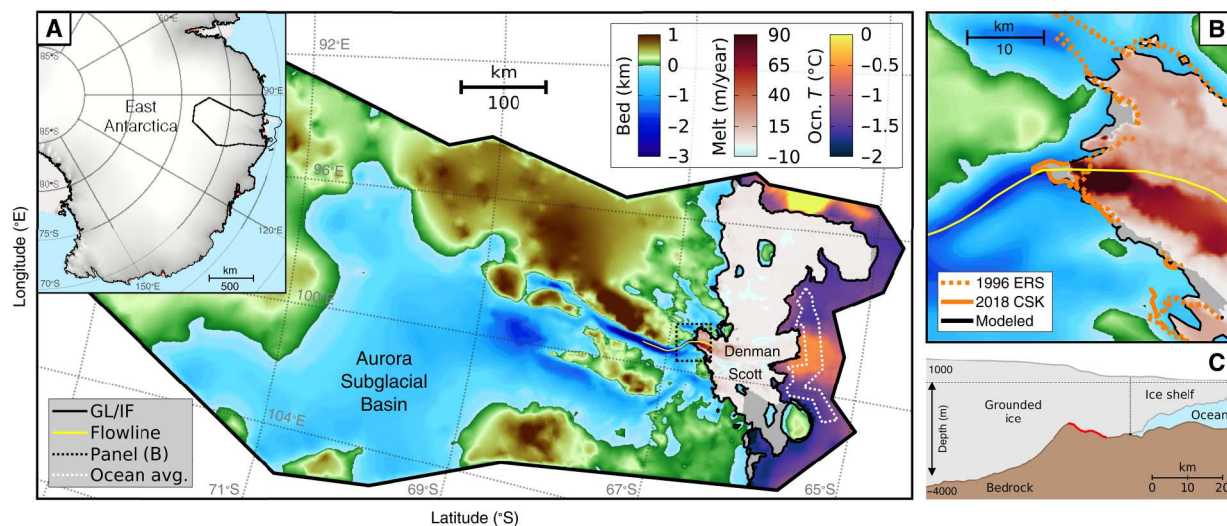*Corresponding author. Email: tpelle@ucsd.edu

Fig. 1. Study area. (**A**) Model domain featuring bed topography (*17*) below grounded ice, satellite inferred ice shelf basal melting rates (*12*) over floating ice, and modeled (*31*) bottom ocean temperature on 1 January 2017 in front of the ice shelf. The yellow flowline is used in (C); the black solid line denotes the initial modeled grounding line and ice front (GL and IF, respectively), and the white dotted line denotes the region over which ocean conditions are averaged. The inset in the top left corner provides a schematic of East Antarctica, where the solid black contour denotes the model domain. (**B**) As in (A) but zoomed into the grounding zone of Denman Glacier, showing observed (*18*) grounding lines at 1996 (dotted orange) and 2018 (solid orange), as well as the initial modeled grounding line (solid black). (**C**) Vertical cross section along the yellow flowline in (A) through Denman Glacier. The red line denotes the region of stabilizing prograde bed topography; the horizontal dashed line denotes sea level, and the vertical dotted line denotes the location of the present-day grounding line.

evolution of Denman and Scott Glaciers (see Materials and Methods). Given the high degree of uncertainty stemming from the prescribed ocean forcing, the ice shelf melt parameterization, and our use of steady-state subglacial conditions, we intend the analysis below to inform the relative sensitivity of Denman and Scott Glaciers to subglacial discharge forcing (not to predict exact dates/rates of change). Furthermore, accelerations in grounding line retreat and ice sheet mass loss discussed below are relative to simulations that do not resolve the discharge melt enhancement.

RESULTS

Subglacial freshwater outflow enhances ice shelf basal melt

Using the Glacier Drainage System (GlaDS) subglacial hydrology model (see Materials and Methods) (*34, 35*) run to steady state at 2017, we simulate subglacial channels discharging freshwater across the grounding lines of Denman and Scott Glaciers (volume flux of 9.50 m^3/s and 4.80 m^3/s, respectively; Fig. 2A). Beneath Denman Glacier, intense channelization of the subglacial freshwater system by the upstream trench leads to the production of a freshwater channel that is routed toward its retreating grounding line. Here, outflowing freshwater into the sub–ice shelf ocean cavity vigorously entrains warm ambient ocean water into the grounding zone, locally enhancing basal melt rates [as has been observed (*22, 24*) forcing the calving fronts of Greenland tidewater glaciers].

Using contemporary observed (*13*) ocean conditions in the melt parameterization developed here (initial temperature and salinity of −1.26°C and 34.67 practical salinity units, respectively), our modeled melt rates display excellent agreement to 2010–2018 average Cryosat-2 satellite inferred melt rates (*12*), where the Denman Glacier grounding zone melt maximum of 126 m/year is captured (Fig. 2). The melt contribution from subglacial discharge

in our parameterization reaches a maximum of ~70 m/year near Denman Glacier's retreating grounding line (Fig. 2C), indicating that subglacial discharge comprises over half of the total modeled melt signal within the grounding zone. Discharge melt enhancements along the Scott Glacier grounding line reach a maximum of ~10 m/year (Fig. 2D) due to the lower discharge subglacial channel draining into the sub–ice shelf cavity, lessened ice shelf basal slopes (*36*) near the discharge outflow location (local slope angle of 0.030 and 0.016 for Denman and Scott Glaciers, respectively), and shallower grounding line depth (−1708 m and −797 m for Denman and Scott Glaciers, respectively).

Grounding line retreat accelerated by subglacial discharge

This strong melting drives widespread and complex patterns of retreat of both glaciers through 2300. In CTRL$_{SD}$ and SSP1-2.6$_{SD}$, the grounding lines of Denman and Scott Glaciers retreat a maximum distance of 8 and 28 km upstream of their present-day locations, respectively, by 2300 (Fig. 3). Under minimal ocean forcing relative to Denman Glacier, the smooth bed underlying Scott Glacier is conducive to widespread retreat that ensues throughout all simulations. Scott Glacier does not retreat along its primary ice stream that is underlain by a subglacial freshwater channel (which would lead to retreat into the eastern entrance of the Aurora Subglacial Basin; dashed gray arrow in Fig. 3A). Instead, retreat progresses through a channel that encircles a topographic high on the western end of the deep upstream trench (solid gray arrow in Fig. 3A). Between 2030 and 2300 in SSP1-2.6$_{SD}$, Scott Glacier's grounding line retreats at an average rate of 0.104 km/year over a smooth bed, while Denman Glacier's grounding line retreats at a rate of only 0.037 km/year

Rapid retreat of Denman Glacier is temporarily hindered by a narrow, 10-km-long section of prograde bed topography (bed that
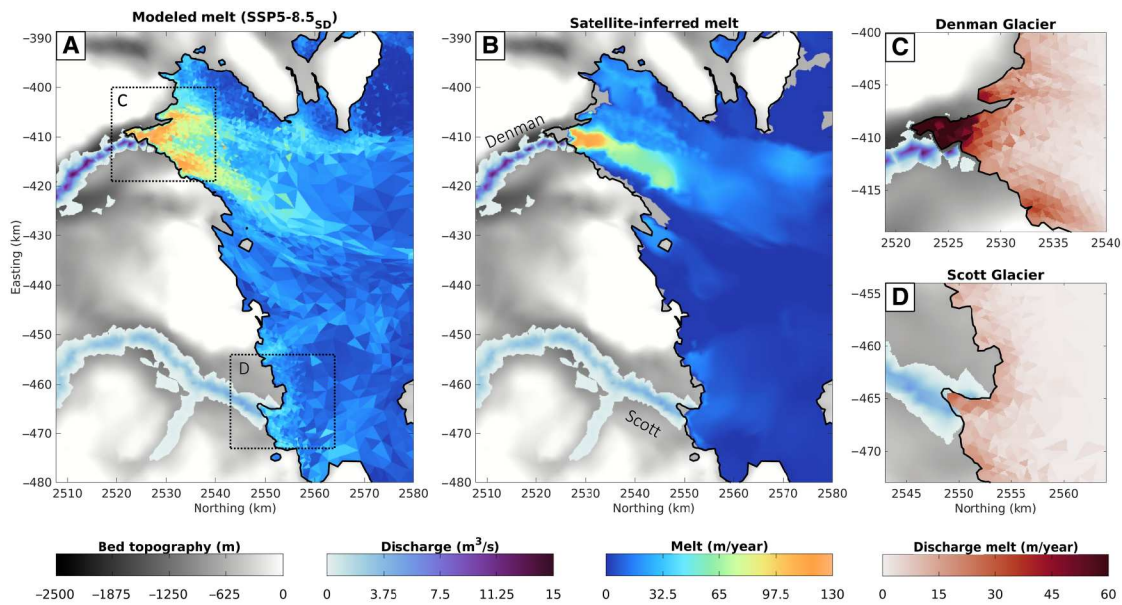
Fig. 2. Modeled and observed ice shelf melt rates. (**A**) Mean 2017–2018 modeled basal melting rates from simulation SSP5-8.5$_{SD}$, (**B**) satellite inferred (*12*) melt rates averaged between 2010 and 2018, and (**C** and **D**) the SSP5-8.5$_{SD}$ melt contribution from subglacial discharge (computed by subtracting the mean 2017–2018 melt fields computed in SSP5-8.5$_{SD}$ from SSP5-8.5$_{NO-SD}$) within the Denman and Scott Glacier grounding zones. Bed topography (*17*) is shaded below grounded ice, and the modeled channelized subglacial discharge flux is overlain. The solid black line denotes the initial modeled grounding line position, and the dotted black rectangles in (A) encompass the domains of (C) and (D).

slopes upward toward the ice sheet interior; red line in Fig. 1C), which the grounding line is not able to retreat past by 2300 in CTRL and SSP1-2.6. In high emission forcing scenarios (SSP5-8.5$_{SD}$ and SSP5-8.5$_{NO-SD}$), however, Denman Glacier retreats past this stabilizing feature, merges with Scott Glacier, and retreats into the upstream subglacial trench. Once the grounding line breaches the trench at year 2235 in SSP5-8.5$_{SD}$, retreat down the retrograde topography and across the 100 km length of the trench takes ~20 years, averaging a retreat rate of 5 km/year during this time (see movie S1). Upstream of the trench, the bedrock becomes prograde and retreat decelerates. By 2300, these two previously independent systems form one floating ice shelf that buttresses the upstream remnants of Denman Glacier.

In all climate forcing scenarios, subglacial discharge accelerates retreat of Denman and Scott Glaciers. By 2300 in both CTRL and SSP1-2.6, Scott and Denman Glaciers retreat an additional 9.50 and 10 km, respectively, under the influence of subglacial discharge relative to the non-subglacial discharge simulations (Fig. 3, B to D). In SSP5-8.5, subglacial discharge accelerates the onset of retreat of Denman and Scott Glaciers into the upstream subglacial trench. By 2240, the combination of intense melt from subglacial discharge and ocean forcing drives retreat of SSP5-8.5$_{SD}$ into the upstream trench, whereas retreat of SSP5-8.5$_{NO-SD}$ to this location is delayed ~25 years (Fig. 3, B to D). Over the time span of this study and for the processes considered here, we find that retreat of Denman and Scott Glaciers is predominantly forced by the ocean, accelerated by subglacial discharge, and controlled by the underlying bed topography.

Global sea level rise

Widespread retreat of Denman and Scott Glaciers results in a varied sea level contribution through 2300. In the control and low

emission scenarios, the discharge and nondischarge simulations either remain in mass balance or slowly gain mass at a maximum rate of −0.01 mm/year sea level change equivalent (SLRe). By 2300, this leads to a sea level contribution between −2.5-mm SLRe (sea level fall) and 0-mm SLRe in all control and low emission simulations. However, in the high emission scenarios, mass loss ensues between 2017 and 2075 at an average rate of 0.01 mm/year SLRe. Between 2075 and 2200, rapid on-shelf ocean warming of ~2°C (fig. S4A) enhances basal melting of the Denman and Scott Glacier ice tongues (Fig. 4A), resulting in increased mass loss at a rate of 0.10 mm/year over this time period. Retreat into the upstream subglacial trench causes an immediate acceleration in mass loss, whereas the rate of the domain's sea level rise contribution temporarily increases to a maximum of 0.33 mm/year SLRe and an average rate of 0.15 mm/year SLRe. This maximum rate of mass loss during retreat across the trench is comparable to approximately half of the present-day sea level rise contribution from the entire Antarctic Ice Sheet (*10*). Once retreat stabilizes on upstream prograde bed topography, mass loss decelerates to a new steady-state rate of ~0.10 mm/year, which is 10 times greater than the domain's present-day rate of mass loss. By 2300, Denman and Scott Glaciers contribute 22-mm SLRe and 19-mm SLRe to global sea levels in SSP5-8.5$_{SD}$ and SSP5-8.5$_{NO-SD}$, respectively.

DISCUSSION

The work presented here stresses the importance of the subglacial environment on the present-day and future evolution of Denman and Scott Glaciers and demonstrates that missing coupled processes between the glacial and subglacial environments in the current generation of ice dynamical models could lead to underestimated future rates of retreat of vulnerable Antarctic glaciers. The magnitude and
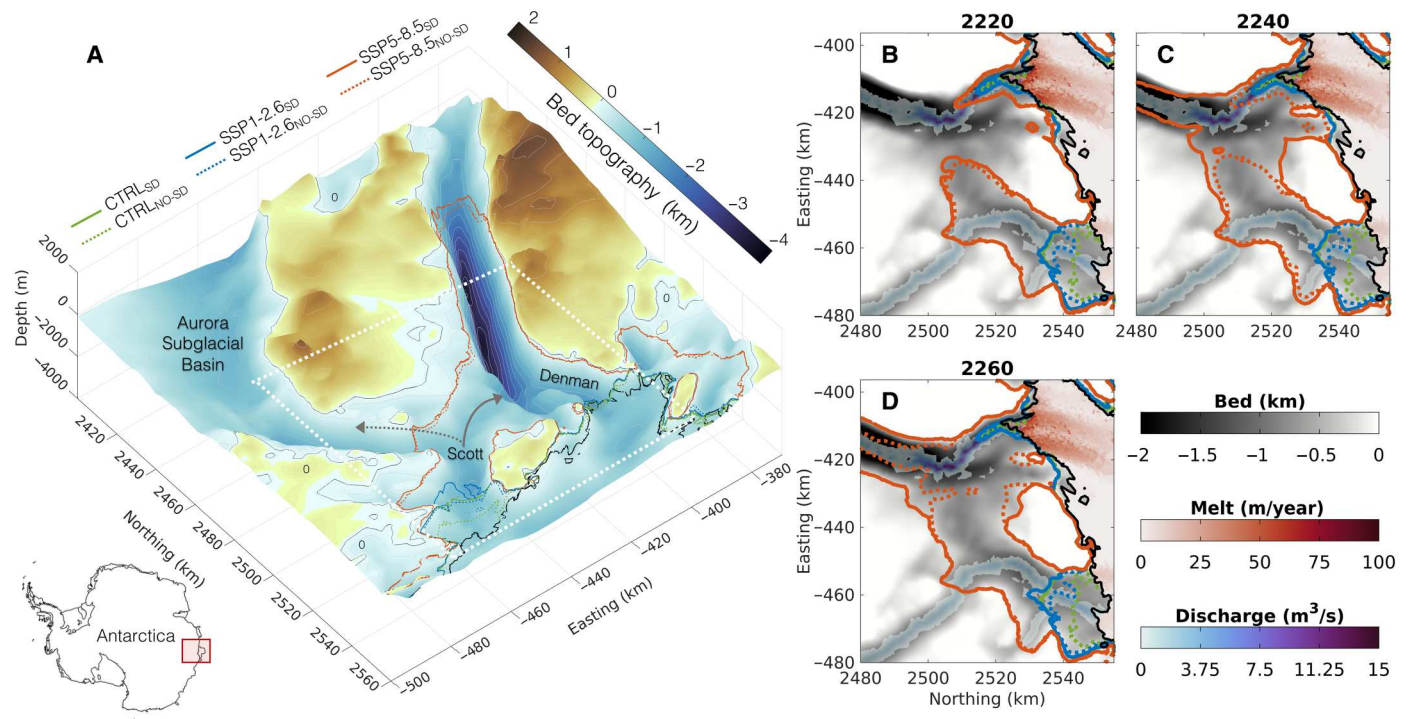
Fig. 3. Future grounding line retreat. (**A**) Modeled 2300 grounding lines overlain onto a three-dimensional surface plot of bed topography (*17*), where solid and dashed lines denote subglacial discharge ($_{SD}$) and non-subglacial discharge ($_{NO-SD}$) simulation results, respectively. The white dotted contour outlines the domain for (B) to (D). The solid and dashed gray arrows denote the realized and expected retreat path of Scott Glacier, respectively. (**B** to **D**) Modeled grounding lines at (B) 2220, (C) 2240, and (D) 2260 overlain onto bed topography and modeled subglacial discharge over grounded ice, and the modeled ice shelf basal melt rate from experiment SSP1-2.6$_{SD}$ at the corresponding year over floating ice. In all panels, the thick black line denotes the present-day modeled grounding line, and thin contours over grounded ice denote sea level (bed topography at 0 m).

localized spatial distribution of the parameterized discharge melt rate enhancements are consistent with three-dimensional ocean modeling studies of the Getz (*28*), Pine Island (*29*), and Totten (*30*) ice shelves. For the Totten Ice Shelf, a system also located in the Aurora Subglacial Basin of East Antarctica, the formation of buoyant plumes sourced from subglacial discharge enhances near-grounding zone melt by up to 40% (*30*). These findings agree with the results presented here despite the highly simplified nature of the melt parameterization relative to a three-dimensional ocean circulation model. While the subglacial discharge melt enhancement is strong within the grounding zone, its highly localized spatial distribution means that the discharge melt signal becomes obscured when basin-mean quantities are considered. This is exemplified in the floating basal mass balance time series (Fig. 4A), in which corresponding time series from simulations that do and do not resolve subglacial discharge are largely superimposed before 2220. However, doubling of the basal melt rate near Denman Glacier's grounding line has broad implications on the stress regime and retreat pattern of the entire upstream grounding glacier, highlighting that considering ice shelf–integrated quantities is not a sufficient way to characterize ice shelf forcing and evolution.

In forward simulations, despite the strong contribution of subglacial discharge to grounding zone ice shelf melt of Denman Glacier, its impact on simulated grounding line retreat relative to corresponding simulations without discharge could be interpreted as seemingly small (25-year difference in the timing of retreat into

the trench and ~10% increase in the 2300 sea level contribution in SSP5-8.5). However, Denman Glacier is a highly buttressed system that is laterally flanked by steep ridges and protected upstream by prograde bed topography (Fig. 1C) (*18*), hindering its retreat. Hence, retreat of Scott Glacier dominates evolution of the domain through 2235; however, discharge fluxes across the Scott Glacier grounding line are small compared to that of Denman Glacier and only drive ice shelf melt enhancements of up to 10 m/year (Fig. 2). Furthermore, there is no modeled discharge flux to enhance ice shelf melt along Scott Glacier's retreat path around the topographic high toward the Denman Ice Stream (solid gray line in Fig. 3A). This means that simulations that do and do not resolve the discharge melt enhancement will experience the same ice shelf forcing as retreat progresses through this region. Although these factors limit the impact of subglacial discharge on retreat of the modeled glaciers, they are also specific to this domain. That is, subglacial hydrology might drive more extensive change of glaciers that are not as highly buttressed (e.g., Thwaites, Pine Island, and Totten Glaciers) or glaciers that experience freshwater discharge forcing along their entire retreat path. Furthermore, the impact of subglacial discharge in the results presented here is likely understated because of the use of 2017 steady-state subglacial conditions.

Rapid undulation of the bed underlying Denman Glacier leads to instability in coupled ice–subglacial hydrology models, rendering the development of a coupled model framework in this region
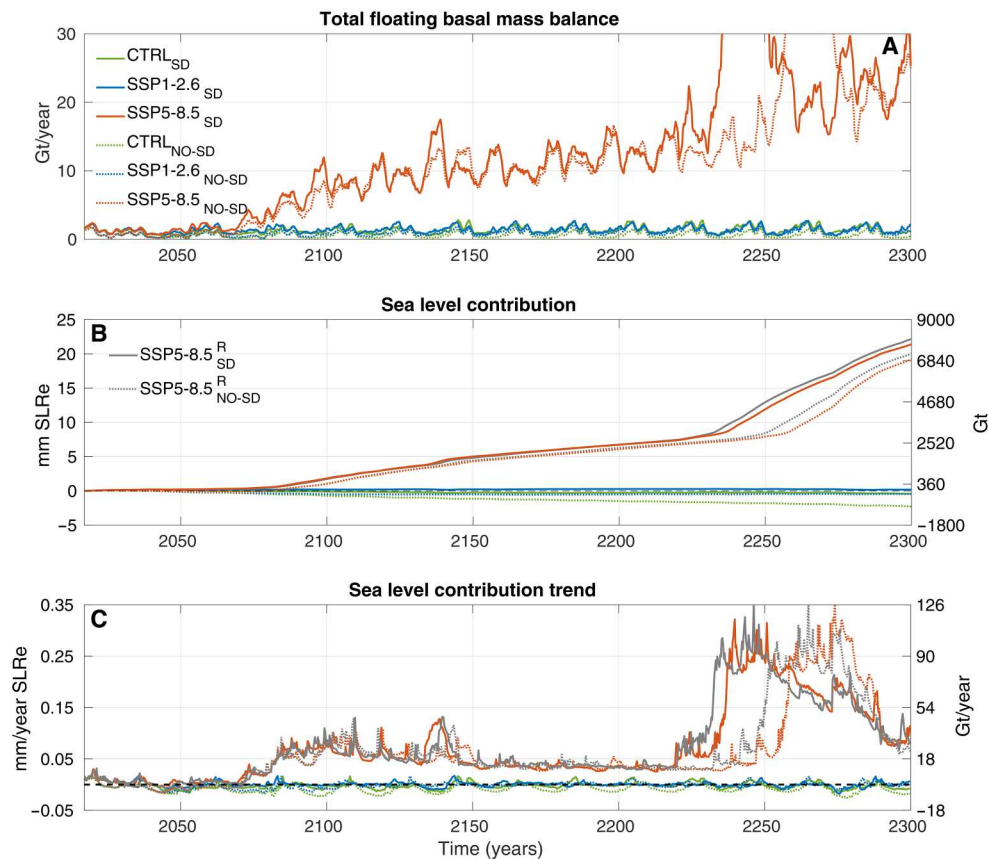
Fig. 4. Ice shelf melt and sea level rise time series. Time series of (**A**) total integrated basal melt within 50 km of the Denman and Scott Glacier grounding line discharge locations, (**B**) domain sea level contribution (positive values indicate sea level rise), and (**C**) the sea level contribution trend computed as the time derivative of the sea level contribution time series through 2300. In all panels, solid and dashed lines denote subglacial discharge ($_{SD}$) and non-subglacial discharge ($_{NO-SD}$) simulations, respectively. Gray lines in (B) and (C) denote results from SSP5-8.5 experiments in which ocean forcing is randomly organized between 2100 and 2300 (see Materials and Methods).

challenging. Hence, we only use present-day subglacial boundary conditions in future simulations (see Materials and Methods); however, coupling to a temporally varying subglacial hydrology model would allow us to account for increased basal water production resulting from enhanced frictional heating (via basal ice acceleration; see movie S1) and surface melt/runoff that can drain to the bed (which is projected to increase across grounded sectors of Antarctica by 2100) (37). Such enhanced rates of basal water production would likely increase the subglacial freshwater flux across the grounding line, further enhancing rates of ice shelf basal melting at deep grounding line locations. For example, in snapshot steady-state simulations of the subglacial freshwater system (see Materials and Methods), we found that the domain-integrated channelized subglacial freshwater flux increased 2.8-fold by 2200 relative to 2017 because of changes in ice geometry and velocity (fig. S10). Furthermore, coupling to a subglacial hydrology model would allow us to resolve fluctuations in subglacial water pressure, which modulate the frictional force at the ice-bed interface that acts to counteract ice sheet sliding. For instance, variations in subglacial water pressure were found to drive seasonal accelerations of the Petermann Glacier, Greenland, of up to 15% (38). As we are unable to account for these time-evolving subglacial processes, we expect Denman and Scott Glaciers to be more vulnerable to subglacial discharge forcing and future climate warming than presented here.

Our results are subject to a high degree of uncertainty sourced from the development of the ice shelf melt parameterization, prescribed ocean forcing, and ice sheet model physics. In this study, we postulate that subglacial discharge can reconcile the uncharacteristically high melt rates recorded near the Denman Glacier grounding line; however, while the melt model developed here resolves the first-order plume dynamics that govern ice shelf melt, it is unable to account for the impact of tidal forcing, Earth rotation, and barotropic water column constraints (see the Supplementary Materials for a full discussion of limitations of the melt model and a sweep of tunable model parameters; figs. S6 and S7). Because we are unable to assess the extent to which these unconstrained mechanisms could influence melting near Denman Glacier's grounding line and because the near-grounding zone ice and seabed geometry are not well characterized, our postulation remains a theory that needs to be tested in a three-dimensional ocean modeling framework and, ideally, with in situ data collection. Similarly, we are unable to account for how subglacial discharge could modulate far-ocean conditions, as we do not couple our models to a dynamic ocean model. Furthermore, the ocean forcing time series were derived by repeating the 20-year forcing cycle of 2079–2099

and extrapolating the warming trend in SSP5-8.5 (see Materials and Methods). This repetition leads to an oscillating cycle of ocean forcing (fig. S4), and to investigate the impact that this might have on retreat into the upstream trench, we perform an additional high emission experiment in which ocean forcing within each 20-year cycle is randomly organized (fig. S8A). While the difference in timing of retreat into the trench between SSP5-8.5$_{SD}$ and SSP5-8.5$_{NO-SD}$ remains similar in these randomized experiments (~25 years), retreat into the trench begins 10 years earlier in both randomized simulations relative to the original simulations (Fig. 4, B and C). That is, the way ocean forcing is prescribed does not substantially modulate the relative impact of subglacial discharge on glacial retreat; however, it does modulate the absolute rate of retreat across all experiments. This highlights that the timing of events in the simulations presented here are dependent on uncertainty in ocean forcing, which is high because we extrapolate far-ocean conditions after 2100, apply artificial warming in SSP5-8.5, and always extract ocean forcing along the present-day ice front. Last, there are several ice sheet model limitations that affect the interpretation of our results, including the choice of basal sliding law, use of a two-dimensional stress balance approximation, and not resolving iceberg calving.

Overall, the simulations presented here provide evidence that a complex subglacial freshwater system underlying the Denman and Scott Glacier catchments can accelerate the onset of their future retreat into the deepest continental trench on Earth. Beyond Denman Glacier, recent modeling and observational studies have inferred the presence of dynamic water systems underlying some of Antarctica's most rapidly melting glaciers [e.g., Thwaites Glacier (25), Pine Island Glacier (29), and Totten Glacier (30)]. These glaciers drain extensive subglacial basins that hold a combined sea level potential of ~5 m in ice above floatation (17) and are vulnerable to future collapse via the Marine Ice Sheet Instability (39–41). As the modeling results presented here show that subglacial discharge can accelerate grounding line retreat, it is likely that this forcing mechanism in combination with warm on-shelf ocean conditions could expedite the irreversible retreat and collapse of these systems. Therefore, it is imperative that future projections of Antarctic glaciers resolve interactions between the ice, ocean, and subglacial environments when in the presence of subglacial outflow.

MATERIALS AND METHODS
Subglacial hydrology modeling
Subglacial hydrology boundary conditions for the domain are modeled with the two-dimensional GlaDS model (34, 35), with the main output used in this study being the channelized discharge (in m^3/s). Distributed flow occurs through linked cavities that are represented as a continuous water sheet of variable thickness modeled on finite elements. Channels grow along finite element edges and exchange water with the adjacent distributed system, as part of a fully coupled two-dimensional drainage network. The model is run up to steady state over 3000 days and has been used to study the basal conditions of ice streams and subglacial lakes in other regions of Antarctica (28, 35, 42). Inputs into GlaDS are the bed and ice surface topography (17) and the basal ice velocity and water production that include both geothermal (43) and frictional sources (computed with ISSM) (33, 44). We do not include the drainage of surface meltwater to the ice-bed interface as an

additional source of basal water because full-depth moulins have not yet been observed in this region in Antarctica. An upper limit of 800 m/year is applied to the basal ice velocity to ensure model stability; this upper limit has not been found to largely influence model output (35). GlaDS output represents the 2017 ice topographic properties of the domain and remains unchanged throughout all simulations (i.e., we do not couple ISSM to GlaDS but rather use the 2017 GlaDS output as a boundary condition in our melt parameterization). Note that discharge fluxes into the sub–ice shelf ocean cavity vary with changes in the position of the grounding line, as the melt parameterization (described below) uses the volume flux of subglacial discharge at a given grounding line position. Steady-state snapshot simulations are performed with the same model setup and basal water production rate as described above; however, input ice geometry and velocity are taken from simulation SSP5-8.5$_{SD}$ at each respective simulation year (fig. S10).

Ice sheet modeling
We model grounded and floating ice dynamics with ISSM (33). The model domain contains all glaciers draining into the Shackleton Ice Shelf and extends inland to the ice divide (Fig. 1A). The domain is discretized into an unstructured triangular mesh that contains 48,449 elements that vary in size between 800 m near ice streams to 40 km in regions of upstream stagnant flow. We refine the mesh within the grounding zones of Denman and Scott Glaciers such that all elements subject to grounding line retreat have a maximum edge length of 800 m to resolve small-scale grounding line and melt processes (45, 46). We integrate forward with a 2-week time step.

The governing ice flow equations are solved through the implementation of the two-dimensional shelfy-stream (47) stress balance approximation to the Stokes flow equations. We initialize our ice sheet model with static inversions of 2017 interferometric synthetic aperture radar (InSAR)–derived surface ice velocities (48) to obtain the basal friction coefficient for grounded elements and ice stiffness coefficient for floating elements (49). These fields remain unchanged throughout all projections. The basal friction coefficient (τ_b) is solved for using a regularized Coulomb friction law (50)

$$\tau_b = \frac{C^2 \cdot |u_b|^{m-1}}{\left[1 + \left(\frac{C^2 \cdot N}{C_{max}}\right)^{1/m} \cdot |u_b|\right]^m} \cdot |u_b| \tag{1}$$

where C is the friction coefficient solved via static inversion, u_b is the basal ice velocity, C_{max} is the Iken's bound (set to 0.8), N is the effective pressure computed as the ice pressure, and m is the friction law exponent (set to $^1/_3$). It has been shown (51) that use of a regularized Coulomb friction law best replicates the recently observed speedup of Pine Island Glacier over a Budd- or Weertman-style friction law and is appropriate for basal sliding over both hard bedrock and soft till. Ice viscosity is computed assuming an ice temperature of −10°C (52). We apply water pressure at the ice-ocean interface, a stress-free boundary condition at the ice-air interface, and constrain inflow boundaries with InSAR-derived surface velocities (48). Bed topography and initial ice geometry are inferred from mass conservation (17), and the present-day surface mass balance field is taken from the Regional Atmospheric Climate Model-2.3 (RACMO2.3p2) (53). We manually lower the bed beneath floating ice to maintain a minimum water column thickness of 300 m near the interior of the

Shackleton Ice Shelf to correct for unobserved grounding of the ice shelf at the initial time step. We use a flotation criterion to determine the position of the grounding line in our model simulations. The precise location of the grounding line within individual elements is tracked using a sub-element grounding line migration parameterization in which basal friction is integrated only over the grounded portion of the element (45). The ice front remains fixed in all projections, as we do not model iceberg calving, and ice shelf basal melting is applied only to elements that are completely floating (46).

The ice shelf melt parameterization is not tuned to match present-day observed (12) basal melt rates in nondischarge experiments, as the Denman Glacier grounding zone melt maximum can only be resolved (without considering discharge) by substantially enhancing the input ocean temperature (figs. S6 and S7). That is, all inputs (T_a and S_a) and parameters (see table S1) within the ice shelf melt parameterization remain consistent between respective experiments.

Experiment forcing

The future simulations are forced by both ocean and subglacial hydrology forcing, which are used as inputs in the ice shelf melt model. We obtain ocean forcing from a regional East Antarctic configuration (31, 54) of the Massachusetts Institute of Technology general circulation model (MITgcm) that spans 90°E to 150°E in longitude and 60°S to 70°S in latitude and has a horizontal resolution of 3 to 4 km. Oceanic and atmospheric boundary conditions were derived from the climatology of the ECCO LLC270 project (55) and ERA-Interim reanalysis (56), respectively, and 2017 initial conditions are generated from a short 25-year spin-up (1992–2016,) (54). The MITgcm is forced at its lateral oceanic boundaries with anomalies in temperature, salinity, and velocity following low and high emission scenarios from the average of four models from the Coupled Model Intercomparison Project phase 6 (CMIP6) (57): CNRM-CM6-1, CNRM-ESM2-1, UKESM1-0-LL, and MIROC-ES2L. These anomalies were taken with respect to year 2017 and are applied to the ocean model boundaries as mean rates of change from 2017 to 2100 at each boundary grid cell (54). Three ocean models were run from 2017 to 2100 by repeating the 1992–2016 boundary and atmospheric forcing and applying the CMIP6 anomalies to the ocean boundaries: (i) CTRL, no anomalies applied to the ocean boundaries; (ii) SSP1-2.6, low emission anomalies applied; and (iii) SSP5-8.5, high emission anomalies applied.

From the three ocean simulations, we extract bimonthly time series of ambient ocean temperature (T_a, °C) and salinity (S_a, units on the practical salinity scale) by averaging these fields along the termini of Denman and Scott Glaciers (white dashed contour in Fig. 1A) through depth from January 2017 to December 2099. Note that ocean conditions are always extracted within this white contour; that is, ocean conditions do not adjust to changing bed topography as grounding line migration ensues. We extrapolate these time series through 2300 by repeating the last 20 years (2079–2099) of modeled forcing (fig. S4). For SSP5-8.5, a strong ocean warming signal appears after 2065, which is caused by a slowdown of the Antarctic Slope Current that acts as a barrier to on-shelf intrusions of modified Circumpolar Deep Water (mCDW) in our model (54). Hence, the 2065–2100 modeled warming trend was extrapolated using a square root function to impose ~2°C warming between 2100 and 2300 (gray line in fig. S4A). Note that we do not linearly extrapolate this warming trend because it would lead to ocean temperatures >8°C by 2300. We do not include a trend in S_a from SSP5-8.5 between 2065 and 2100, as no trend was evident in the salinity output during this time period. Last, we take anomalies of these time series with respect to the first decade of forcing (2017–2027) and add them to the mean in situ observations detailed in the introduction (−1.26°C and 34.67 units on the practical salinity scale) (13) to remove dependence on the initial state of our ocean models. We note that ocean T_a and S_a in CTRL and SSP1-2.6 remain similar through 2300 because there was minimal variation in the SSP1-2.6 CMIP6 anomalies (figs. S3 to S6) (54).

In addition, we obtain subglacial hydrology forcing from the 2017 steady-state, channelized subglacial flux output modeled with GlaDS over the domain. This two-dimensional flux field remains unchanged throughout each simulation, as we are not dynamically coupling ISSM to GlaDS; however, as grounding line migration ensues, the flux and channel width at the new grounding line position may be different from the initial time step (i.e., the modeled flux of subglacial water into the sub–ice shelf ocean cavity will change with the position of the grounding line). As the melt parameterization developed here only considers the volume flux of freshwater at the grounding line, subglacial discharge under floating ice is set to 0 m³/s.

Melt rate parameterization

Ice shelf basal melting is parameterized in our ice sheet model using a two-dimensional meltwater plume parameterization (14) that is modified near grounding line subglacial freshwater outflow locations to account for the additional source of buoyancy via a widely applied discharge plume model (32). The meltwater plume melt parameterization (14) was developed on the basis of the assumption that the main physical mechanism driving the ocean circulation within the ocean cavity is the positive buoyancy of ice shelf meltwater, which travels along the ice shelf–ocean interface in the form of a turbulent plume from the grounding line up to the point where the plume loses buoyancy. Meltwater plume dynamics are driven by ambient ocean temperature and salinity and the geometry of the sub–ice shelf ocean cavity (namely, the grounding line depth field and ice shelf basal slopes, both described below). This parameterization was applied to the whole Antarctic Ice Sheet and was found to reproduce the complex spatial distribution and magnitude of ice shelf melt rates reasonably well (14).

Near grounding line subglacial discharge locations, however, the outflow of subglacial freshwater constitutes an additional source of buoyancy and convection that can drive entrainment of warm ambient ocean water into the grounding zone, locally enhancing melt up to the point at which buoyancy becomes dominated by the input of ice shelf melt water. Hence, near grounding line subglacial discharge locations, we modify the plume parameterization with a two-dimensional implementation of the discharge plume model (32), which is derived from the same governing equations as the meltwater plume model. Within the region where subglacial drainage dominates buoyancy forcing, ice shelf melt rates still maintain a complex dependence on the geometry of the sub–ice shelf cavity and ambient ocean conditions as described above; however, melt is additionally proportional to the volume flux of subglacial water that is ejected into the ice shelf cavity. Furthermore, the

extent of the region over which subglacial discharge controls plume buoyancy is also proportional to the subglacial volume flux.

To construct this parameterization, the two-dimensional meltwater plume parameterization is applied across the entire ice shelf. Near grounding line discharge locations, we first solve for the distance over which discharge dominates plume dynamics and, within this distance, apply the discharge plume melt formulation. This parameterization provides us with a melt field that is defined on every completely floating ice shelf mesh element and accounts for the localized melt enhancement resulting from subglacial discharge. We emphasize that both the meltwater and discharge plume parameterizations were derived in previous work [(14) and (32), respectively]. However, the discharge plume parameterization was only derived for use along a flowline (one dimension). Thus, the way both parameterizations are combined and implemented into an ice sheet model is a new contribution. Note that all constants and fields below are defined in table S1.

Meltwater plume melt rate parameterization

The two-dimensional plume ice shelf basal melt rate parameterization (14) is based on the one-dimensional theory of buoyant meltwater plumes (2). Here, plumes originate at the grounding line and travel upward along the base of the ice shelf, inducing melt up to the ice front or to the point at which the current loses buoyancy. The plume's trajectory is controlled primarily by the ambient ocean temperature and salinity (T_a and S_a, respectively), the local slope angle of the ice shelf draft (α), and the depth at which the plume originated that reaches a particular shelf point (z_{gl}). The only source of buoyancy the plume gains throughout its trajectory is from the input of cold, fresh ice shelf melt water. Below, we provide a brief overview of the equations governing the buoyant plume parameterization but point readers to the original publication (14) for a complete derivation. All variables used in the derivation of the melt model are defined in table S1.

From ice shelf geometry and ambient ocean data, we are supplied with the ice shelf draft z_b (which also provides us with z_{gl} and α) and basin-averaged T_a and S_a. Now, α and z_{gl} are two-dimensional fields that vary spatially and are defined on every completely floating ice mesh element. We obtain α from the ice shelf draft, which is computed as the maximum slope angle at every floating mesh element. Solving for z_{gl} is still an active area of research and has been previously computed by searching for valid plume origins at every ice shelf point (14) and by advection of the depths of the grounding line with the modeled surface ice velocity (19). Here, we choose the latter approach, as it decreases computational expense and has already been implemented in ISSM. First, we define the depth-dependent freezing point of the plume ($\Delta T_{f,gl}$, in meters)

$$\Delta T_{f,gl} = \frac{T_a - \lambda_1 S_a + \lambda_2 + \lambda_3 z_{gl}}{\lambda_3} \qquad (2)$$

where λ_1, λ_2, and λ_3 are constant parameters defined in table S1. In this model, melting is driven by the difference between T_a and $\lambda_1 S_a + \lambda_2 + \lambda_3 z_{gl}$, which is captured by this factor. Next, we define the empirically derived effective heat exchange coefficient (dimensionless)

$$\Gamma_{TS} = \Gamma_T \cdot \left[\gamma_1 + \gamma_2 \Delta T_{f,gl} \cdot \frac{E_0 \sin(\alpha)}{C_d^{1/2} \Gamma_{Ts_0} + E_0 \sin(\alpha)} \right] \qquad (3)$$

where Γ_T, γ_1, γ_2, E_0, and $C_d^{1/2} \Gamma_{Ts_0}$ are constants defined in table S1. Thus, Γ_{TS} is an empirical function that relates Γ_T with $\Delta T_{f,gl}$ and scales melt rates along the plume path.

We define the dimensionless geometrical factors that give the plume model the proper scaling with distance along the plume path. We define G_1 (plume temperature scaling above freezing point, which scales heat transfer to the ice shelf base; described above), G_2 (plume speed scaling), and G_3 (plume temperature scaling relative to T_a, which scales plume buoyancy)

$$G_1 = \frac{E_0 \sin(\alpha)}{C_d^{1/2} \Gamma_{TS} + E_0 \sin(\alpha)} \qquad (4)$$

$$G_2 = \frac{\sin(\alpha)}{C_d + E_0 \sin(\alpha)} \qquad (5)$$

$$G_3 = \frac{C_d^{1/2} \Gamma_{Ts_0}}{C_d^{1/2} \Gamma_{Ts_0} + E_0 \sin(\alpha)} \qquad (6)$$

G_2 scales the plume speed by accounting for the ratio of the plume buoyancy to frictional drag. G_3 is a factor that scales the plume temperature relative to the ambient ocean temperature T_a and thus controls plume buoyancy. These factors are derived empirically in appendix A of (14) and are described in further detail in section 2.2 of (14).

G_1, G_2, and G_3 are combined to provide us with the universal geometric scaling factor $G(\alpha)$

$$G(\alpha) = G_1 \cdot G_2^{1/2} \cdot G_3^{1/2} \qquad (7)$$

Next, we compute the dimensionless coordinate $\hat{X}$ that is measured from the grounding line over which the universal melt rate scaling is applied

$$L = \Delta T_{f,gl} \cdot \frac{x_o \Gamma_{TS} + E_0 \sin(\alpha)}{x_o [\Gamma_{TS} + E_0 \sin(\alpha)]} \qquad (8)$$

$$\hat{X} = \frac{z_b - z_{gl}}{L} \qquad (9)$$

$x_o = 0.56$ sets the transition point from melting to refreezing in the buoyant plume model along a dimensionless coordinate system $\hat{X}$ (defined above). $\hat{X}$ is the coordinate system over which the plume model is applied and ranges from 0 to 1. Note that $\hat{X} = 0$ corresponds to the position of the grounding line and $\hat{X} = 0.56$ corresponds to the aforementioned melting-refreezing transition point, but $\hat{X} = 1$ does not necessarily correspond to the calving front because of the dependence of $\hat{X}$ on L. To ensure valid values of $\hat{X}$, we set a lower bound on the ambient ocean temperature: $T_a > \lambda_1 S_a + \lambda_2$, which gives $\hat{X} = 1$ at the sea surface.

Last, we compute the empirical melt rate scale M (dimensionless) and universal melt curve $M(\hat{X})$ (in m/year) that, when

combined, provide us with the final melt rate field m_o (in m/year)

$$M = M_0 \cdot G(\alpha) \cdot (\lambda_3 \cdot \Delta T_{f,gl})^2 \tag{10}$$

$$M(\hat{X}) = \sum_{k=1}^{11} p_k \cdot \hat{X}^k \tag{11}$$

$$m_o = M \cdot M(\hat{X}) \tag{12}$$

where coefficients p_k are provided in the corrigendum of the original publication (14) and M_0 is a constant defined in table S1. $M(\hat{X})$ is a universal Antarctic melt curve (14) that reaches a maximum of 2 at $\hat{X} \approx 0.2$ and transitions from positive (melting) to negative (refreezing) at $\hat{X} = 0.56$ (as described above).

Melt rates computed with Eq. 12 have a quadratic dependence on the ocean thermal forcing and have been validated on numerous idealized and realistic geometries (14, 16). However, as the modeled plume is only driven by buoyancy gained by melt water input, melting approaches zero at the grounding line, as there is no source of buoyancy and the plume thickness approaches zero. While this assumption is acceptable when only considering ice-ocean coupled systems, the discharge of fresh subglacial water across the grounding line and into the sub–ice shelf cavity provides an alternative source of buoyancy and convection at the grounding line. This source of buoyancy can drive entrainment of warm ambient ocean water into the plume in contact with the ice-ocean interface near the grounding line, locally enhancing melt up to the point at which buoyancy is dominated by melt water derived from the ice shelf. That is, the melt model defined above will be invalid close to where fresh subglacial discharge flows into the sub–ice shelf cavity because plume dynamics will be governed by the initial source of buoyancy rather than that generated by melting.

Modification to include subglacial discharge melt enhancement

Here, we first provide a description of the equations governing ice shelf melt under the influence of subglacial discharge, which was previously derived [equation 40 in (32)]. We then provide details of the length scale that determines how far from the discharge channel plume dynamics are governed by subglacial discharge [table 3 in (32)]. Last, we provide the final expression to combine melt from the buoyant plume model (Eq. 12) with the convective plume model (Eq. 14) to arrive at our final melt solution. We provide a full derivation of Eqs. 13 and 15 in the Supplementary Materials. To begin, we use previously published results (32) to compute the melt rate field driven by the subglacial outflow

$$m_{fw} = 31{,}536{,}000 \cdot \frac{1}{L/c_p} \cdot G_1 \cdot G_2^{1/3} \cdot C_d^{1/2} \Gamma_{Ts_0}$$
$$\cdot (g \cdot q_{sg} \cdot \Delta\rho_i)^{1/3} \cdot (\lambda_3 \cdot \Delta T_{f,gl}) \tag{13}$$

where 31,536,000 (in s/year) is a conversion factor from m/s to m/year. Now, assuming that the second factor in Eq. 13 is approximately equal to 0.01°C^{-1}, $C_d^{1/2}\Gamma_{Ts_0} = 6 \cdot 10^{-4}$ (dimensionless) and

combining $g^{1/3}$ with the leading coefficient, we get

$$m_{fw} = 405 \cdot G_1 \cdot G_2^{\frac{1}{3}} \cdot (q_{sg} \cdot \Delta\rho_i)^{\frac{1}{3}} \cdot (\lambda_3 \cdot \Delta T_{f,gl}) \tag{14}$$

where the factor of 405 has units m$^{1/3}$ s$^{1/3}$ °C^{-1} year^{-1} and q_{sg} is the subglacial discharge flux in units of m^2 s^{-1} defined on all floating ice mesh elements (see the next section). Now, $\Delta\rho_i$ is the density contrast between ambient ocean waters and waters that occupy the plume. This is originally defined as $\Delta\rho_i = \beta_s(S_a - S) - \beta_t(T_a - T)$ (32), where T and S are the temperature and salinity of the plume waters, respectively. Here, we assume that $S = 0$ (subglacial discharge is fresh) and $T_a - T \approx \lambda_3 \cdot \Delta T_{f,gl}$, providing us with $\Delta\rho_i = \beta_s S_a - \beta_t(\lambda_3 \cdot \Delta T_{f,gl})$ (dimensionless). As in the meltwater plume model, melt rates are provided a complex geometry dependence through factors G_1 and G_2, described in the previous section. Furthermore, we observe that melting near the grounding line under the influence of subglacial discharge scales to the one-third power of the discharge flux and linearly with ocean thermal forcing. The exponent scaling the subglacial discharge flux (q_{sg}) has been the focus of recent literature (22) and was found to underestimate melt rates on vertical ice cliffs in the presence of ocean stratification. However, we are focused on simulating melt rates at the near-horizontal bases of Antarctic ice shelves, where the one-third exponent has been found (22, 30) to provide reasonable results under a variety of ocean and discharge forcing conditions. The melt formulation above is valid over the domain where the buoyancy from subglacial discharge dominates that from melting. For typical Antarctic ice shelves where the sine of the local slope angle is ~0.01, this length scale is defined as

$$5L' = \frac{500 \cdot q_{sg}^{2/3}}{(g \cdot \Delta\rho_i)^{1/3} \cdot C_d^{1/2}\Gamma_{Ts_0} \cdot G_1 \cdot G_2^{1/3} \cdot (\lambda_3 \cdot \Delta T_{f,gl})} \tag{15}$$

where $\Delta\rho_i$ is as defined above, 500 arises from the simplification of 5 $\cdot (L/c_w) \approx 5 \cdot 100 = 500$ (in °C), and quantities are averaged within 5 km downstream of discharge outflow location. The distance of 5 km was chosen because the maximum edge length of all floating mesh elements in the domain is ~5 km, so we can be sure we are averaging quantities over at least one mesh element. The quantity $5L'$ (in m) is known as the governing length scale and sets the distance in meters from the grounding line discharge location at which plume dynamics become primarily driven by the buoyancy input from melting rather than subglacial discharge. That is, for every grounding line outflow location, $5L'$ sets the radius from the discrete discharge location over which q_{sg} on floating mesh elements is nonzero. Thus, m_{fw} is defined across all ice shelf mesh elements but is only nonzero within $5L'$ meters from the discharge location. We combine the two melt parameterizations with an additive interpolation scheme

$$m = \left[\frac{M(\hat{X}) \cdot M^2}{M + m_{fw}} \right] + m_{fw} \tag{16}$$

On floating elements where $m_{fw} = 0$ (i.e., beyond $5L'$ from the discharge channel where $q_{sg} = 0$ m^2/s), the melt solution defaults to m_o (Eq. 12). On floating elements where $m_{fw} \neq 0$, the expression above provides enhanced melting near the discharge source location as defined by Eq. 14 and smoothly transitions to the ocean melting regime beyond $5L'$. We use an additive interpolation scheme to combine the meltwater and discharge plume models because melting near the grounding line is driven by the amount of heat

that is entrained into the plume. Entrainment is directly proportional to the speed of the plume: $e = E_0 \bullet U \bullet \sin(\alpha)$, where e is the entrainment rate and U is the plume speed, which is determined by its buoyancy. If buoyancy is added to the plume (i.e., freshwater outflow at the grounding line), then speed and, hence, heat are also added. That is, the buoyancy (and resultant heat from additional entrainment) that is supplied to the plume via freshwater outflow is added to that which is sourced from meltwater, thus driving ice shelf melt.

Defining the ice shelf discharge flux field $q_{sg}(x, y)$

The melt formulation defined above was originally adapted for use in a one-dimensional plume model, where the subglacial discharge flux is a point source at the grounding line represented by a scalar (*32*). In two dimensions, grounding lines can be extensive and there can be multiple subglacial channels with varying fluxes draining into the same sub–ice shelf ocean cavity, complicating the two-dimensional application of this field. To address this, we define $q_{sg}(x, y)$ to be a spatially varying field that is defined on all completely floating ice shelf mesh elements.

To do this, we use channelized subglacial flux output (FW_{sg}, m³/s) from the two-dimensional GlaDS model over our model domain (Fig. 2, A and B, white to purple shading over grounded ice). With FW_{sg}, we first extract the flux values along the grounding line, providing us with both the grounding line discharge field and the horizontal distance along the grounding line (fig. S2A). From here, we can obtain the domain-mean "channel width" of the subglacial channels draining across the grounding line, which we define as the point-to-point distance where the subglacial discharge flux is greater than or equal to 2 m³/s across the grounding line. We decided to use this method to determine the channel width because ISSM runs on an unstructured triangular mesh and uses a sub-element grounding line migration parameterization, so the exact position of the grounding line is often not located on mesh nodes. However, if one is implementing this parameterization in an ice sheet model that runs on a regular grid, then one could divide the grounding line discharge volume flux by the width(s) of the grid cell(s) over which discharge is defined. The regions over which the grounding line subglacial flux exceeds this threshold for Denman and Scott Glaciers are shaded in red in fig. S2A. We then divide FW_{sg} by the domain-mean channel width to obtain the channelized subglacial discharge flux in units of m²/s, which is required for use in the melt parameterization.

For each grounding line discharge location, we then extract the maximum freshwater flux value and compute $5L'$ using averaged fields (e.g., α, z_{gl}, etc.) within 5 km from the discharge outflow location (see the previous section for reasoning). For a given discharge outflow location, we use $5L'$ to define a radius around the grounding line discharge channel. We set $q_{sg}(x, y)$ equal to the maximum flux value at the discharge outflow location, $q_{sg}(x, y) = 0$ beyond $5L'$ and over grounded ice, and $q_{sg}(x, y)$ decays quadratically between the discharge outflow location and $5L'$. We accomplish this by first defining a relative distance mask ($mask_{dist}$) that is equal to 1 at the discharge location and experiences quadratic decay to 0 at $5L'$ (fig. S2B). We also construct a second discharge mask ($mask_{dis}$) that is simply set to the maximum discharge flux value across all floating mesh elements where $mask_{dist} \neq 0$ (fig. S2C). Last, we multiply these masks together to get $q_{sg}(x, y)$ (fig. S2D) and use this as an input into the melt parameterization to get m (fig. S2E). The choice to apply

quadratic decay to $q_{sg}(x, y)$ is an assumption made in the derivation of this parameterization, as it makes a statement on how the impact of subglacial discharge dissipates with distance from the grounding line outflow location. However, we would largely expect quadratic decay from uniform radial spreading of the freshwater discharge from the outflow location, and this assumption provided the best match to idealized case studies (figs. S1 and S3). Furthermore, this is the best that can be done without making an assumption about the direction that the outflow travels in. This method also effectively conserves the mass flux of the discharge. Please see the Supplementary Materials for a discussion on the validation and limitations of this parameterization.

Supplementary Materials

This PDF file includes:
Supplementary Text
Table S1
Figs. S1 to S10
Legend for movie S1

Other Supplementary Material for this manuscript includes the following:
Movie S1

REFERENCES AND NOTES

1. E. L. Lewis, R. G. Perkin, Ice pumps and their rates. *J. Geophys. Res.* **91**, 11756–11762 (1986).
2. A. Jenkins, A one-dimensional model of ice shelf-ocean interaction. *J. Geophys. Res.* **96**, 20671–20677 (1991).
3. E. Rignot, S. Jacobs, J. Mouginot, B. Scheuchl, Ice-shelf melting around Antarctica. *Science* **341**, 266–270 (2013).
4. H. D. Pritchard, H. A. Fricker, D. G. Vaughan, M. R. van den Broeke, L. Padman, Antarctic ice-sheet loss driven by basal melting of ice shelves. *Nature* **484**, 502–505 (2012).
5. F. S. Paolo, H. A. Fricker, L. Padman, Volume loss from Antarctic ice shelves is accelerating. *Science* **348**, 327–331 (2015).
6. C. A. Greene, A. S. Gardner, N. J. Schlegel, A. D. Fraser, Antarctic calving loss rivals ice-shelf thinning. *Nature* **609**, 948–953 (2022).
7. S. Jacobs, A. Jenkins, H. Hellmer, C. Giulivi, F. Nitsche, B. Huber, R. Guerrero, The Amundsen Sea and the Antarctic Ice Sheet. *Oceanography* **25**, 154–163 (2012).
8. A. Shepherd, E. Ivins, E. Rignot, B. Smith, M. van den Broeke, I. Velicogna, P. Whitehouse, K. Briggs, I. Joughin, G. Krinner, S. Nowicki, T. Payne, T. Scambos, N. Schlegel, A. Geruo, C. Agosta, A. Ahlstrøm, G. Babonis, V. Barletta, A. Blazquez, J. Bonin, B. Csatho, R. Cullather, D. Felikson, X. Fettweis, R. Forsberg, H. Gallee, A. Gardner, L. Gilbert, A. Groh, B. Gunter, E. Hanna, C. Harig, V. Helm, A. Horvath, M. Horwath, S. Khan, K. K. Kjeldsen, H. Konrad, P. Langen, B. Lecavalier, B. Loomis, S. Luthcke, M. M. Millan, D. Melini, S. Mernild, Y. Mohajerani, P. Moore, J. Mouginot, G. Moyano, A. Muir, T. Nagler, G. Nield, J. Nilsson, B. Noel, I. Otosaka, M. E. Pattle, W. R. Peltier, N. Pie, R. Rietbroek, H. Rott, L. Sandberg-Sørensen, I. Sasgen, H. Save, B. Scheuchl, E. Schrama, L. Schröder, K.-W. Seo, S. Simonsen, T. Slater, G. Spada, T. Sutterley, M. Talpe, L. Tarasov, W. J. van de Berg, W. van der Wal, M. van Wessem, B. D. Vishwakarma, D. Wiese, B. Wouters, Mass balance of the Antarctic Ice Sheet from 1992 to 2017. *Nature* **558**, 219–222 (2018).
9. A. Jenkins, D. Shoosmith, P. Dutrieux, S. Jacobs, T. W. Kim, S. H. Lee, H. K. Ha, West Antarctic Ice Sheet retreat in the Amundsen Sea driven by decadal oceanic variability. *Nat. Geosci.* **11**, 733–738 (2018).
10. E. Rignot, J. Mouginot, B. Scheuchl, M. van den Broeke, M. J. van Wessem, M. Morlighem, Four decades of Antarctic Ice Sheet mass balance from 1979–2017. *Proc. Natl. Acad. Sci.* **116**, 1095–1103 (2019).
11. B. Smith, H. A. Fricker, A. S. Gardner, B. Medley, H. Nilsson, F. S. Paolo, N. Holschuh, S. Adudumilli, K. Brunt, B. Csatho, K. Harbeck, T. Markus, T. Neumann, M. R. Siegfried, H. Z. Zwally, Pervasive ice sheet mass loss reflects competing ocean and atmosphere processes. *Science* **368**, 1239–1242 (2020).
12. S. Adusumilli, H. A. Fricker, B. Medley, L. Padman, M. R. Siegfried, Interannual variations in meltwater input to the Southern Ocean from Antarctic ice shelves. *Nat. Geosci.* **13**, 616–620 (2020).

13. A. Treasure, F. Roquet, I. J. Ansorge, M. N. Bester, L. Boehme, H. Bornemann, J. Charrassin, D. Chevallier, D. P. Costa, M. A. Fedak, C. Guinet, M. O. Hammill, R. G. Harcourt, M. A. Hindell, K. M. Kovacs, M. Lea, P. Lovell, A. D. Lowther, C. Lydersen, T. McIntyre, C. R. McMahon, M. M. C. Muelbert, K. Nicholls, B. Picard, G. Reverdin, A. W. Trites, G. D. Williams, P. J. Nico de Bruyn, Marine mammals exploring the oceans pole to pole: a review of the MEOP consortium. *Oceanography* **30**, 132–138 (2017).

14. W. M. J. Lazeroms, A. Jenkins, G. H. Gudmundsson, R. S. W. van de Wal, Modelling present-day basal melt rates for Antarctic ice shelves using a parametrization of buoyant meltwater plumes. *Cryosphere* **12**, 49–70 (2018).

15. R. Reese, T. Albrecht, M. Mengel, X. Asay-Davis, R. Winkelmann, Antarctic sub-shelf melt rates via PICO. *Cryosphere* **12**, 1969–1985 (2018).

16. T. Pelle, M. Morlighem, J. H. Bondzio, Brief communication: PICOP, a new ocean melt parameterization under ice shelves combining PICO and a plume model. *Cryosphere* **13**, 1043–1049 (2019).

17. M. Morlighem, E. Rignot, T. Binder, D. Blankenship, R. Drews, G. Eagles, O. Eisen, F. Ferraccioli, R. Forsberg, P. Fretwell, V. Goel, J. S. Greenbaum, H. Gunmundsson, J. Guo, V. Helm, C. Hofstede, I. Howat, A. Humbert, W. Fokat, N. B. Karlsson, W. S. Lee, K. Matsuoka, R. Millan, J. Mouginot, F. Paden, F. Pattyn, J. Roberts, S. Rossier, A. Ruppel, H. Seroussi, E. C. Smith, D. Steinhage, B. Sun, M. R. van den Broeke, T. D. van Ommen, M. van Wessem, D. A. Young, Deep glacial troughs and stabilizing ridges unveiled beneath the margins of the Antarctic ice sheet. *Nat. Geosci.* **13**, 132–137 (2020).

18. V. Brancato, E. Rignot, P. Milillo, M. Morlighem, J. Mouginot, L. An, B. Scheuchl, S. Jeong, R. Rizzoli, L. B. Bello, P. Prats-Iraola, Grounding line retreat of Denman Glacier, East Antarctica, measured with COSMO-SkyMed radar interferometry data. *Geophys. Res. Lett.* **47**, e86291 (2020).

19. B. W. J. Miles, J. R. Jordan, C. R. Stokes, S. S. R. Jamieson, H. Gudmundsson, A. Jenkins, Recent acceleration of Denman Glacier (1972–2017), East Antarctica, driven by grounding line retreat and changes in ice tongue configuration. *Cryosphere* **15**, 663–676 (2021).

20. M. J. Fried, G. A. Catania, T. C. Bartholomaus, D. Duncan, M. Davis, L. A. Stearns, J. Nash, E. Shroyer, D. Sutherland, Distributed subglacial discharge drives significant submarine melt at a Greenland tidewater glacier. *Geophys. Res. Lett.* **42**, 9328–9336 (2015).

21. R. Sciascia, F. Straneo, C. Cenedese, P. Heimbach, Seasonal variability of submarine melt rate and circulation in an East Greenland fjord. *J. Geophys. Res.* **118**, 2492–2506 (2013).

22. D. A. Slater, P. W. Nienow, T. R. Cowton, D. N. Goldberg, A. J. Sole, Effect of near-terminus subglacial hydrology on tidewater glacier submarine melt rates. *Geophys. Res. Lett.* **42**, 2861–2868 (2015).

23. S. J. Cook, P. Christoffersen, J. Todd, D. A. Slater, N. Chauché, Coupled modelling of subglacial hydrology and calving-front melting at Store Glacier, West Greenland. *Cryosphere* **14**, 905–924 (2020).

24. A. Everett, T. Murray, N. Selmes, D. Holland, D. E. Reeve, The impacts of a subglacial discharge plume on calving, submarine melting, and mélange mass loss at Helheim Glacier, South East Greenland. *Case Rep. Med.* **126**, e2020JF005910 (2021).

25. A. P. Lepp, L. M. Simkins, J. B. Anderson, R. W. Clark, J. S. Wellner, C. D. Hillenbrand, J. A. Smith, A. A. Lehrmann, R. Totten, R. D. Larter, K. A. Hogan, F. O. Nitsche, A. G. C. Graham, L. Wacker, Sedimentary signatures of persistent subglacial meltwater drainage from Thwaites Glacier, Antarctica. *Front. Earth Sci.* **10**, 863200 (2022).

26. A. M. Le Brocq, N. Ross, J. A. Griggs, R. G. Bingham, H. F. J. Corr, F. Ferraccioli, A. Jenkins, T. A. Jordan, A. J. Payne, D. M. Rippin, M. H. Seigert, Evidence from ice shelves for channelized meltwater flow beneath the Antarctic Ice Sheet. *Nat. Geosci.* **6**, 945–948 (2013).

27. K. E. Alley, T. A. Scambos, M. R. Siegfried, H. A. Fricker, Impacts of warm water on Antarctic ice shelf stability through basal channel formation. *Nat. Geosci.* **9**, 290–293 (2016).

28. W. Wei, D. D. Blankenship, J. S. Greenbaum, N. Gourmelen, C. F. Dow, T. G. Richter, C. A. Green, D. A. Young, S. Lee, T. Kim, W. S. Lee, K. M. Assmann, Getz Ice Shelf melt enhanced by freshwater discharge from beneath the West Antarctic Ice Sheet. *Cryosphere* **14**, 1399–1408 (2020).

29. Y. Nakayama, C. Cai, H. Seroussi, Impact of subglacial freshwater discharge on Pine Island Ice Shelf. *Geophys. Res. Lett.* **48**, e93923 (2021).

30. D. Gwyther, C. Dow, S. Jendersie, N. Gourmelen, B. Galton-Fenzi, Subglacial freshwater drainage increases simulated basal melt of the totten ice shelf. *Geophys. Res. Lett.* **50**, e2023GL103765 (2023).

31. Y. Nakayama, C. A. Green, F. S. Paolo, V. Mensah, H. Zhang, H. Kashiwase, D. Simizu, J. S. Greenbaum, D. D. Blankenship, A. Abe-Ouchi, S. Aoki, Antarctic slope current modulates ocean heat intrusions towards totten glacier. *Geophys. Res. Lett.* **48**, e2021GL094149 (2021).

32. A. Jenkins, Convection-driven melting near the grounding lines of ice shelves and tidewater glaciers. *J. Phys. Oceanogr.* **41**, 2279–2294 (2011).

33. E. Larour, H. Seroussi, M. Morlighem, E. Rignot, Continental scale, high order, high spatial resolution, ice sheet modeling using the Ice Sheet System Model (ISSM). *J. Geophys. Res.* **117**, F01022 (2012).

34. M. A. Werder, I. J. Hewitt, C. G. Schoof, G. E. Flowers, Modeling channelized and distributed subglacial drainage in two dimensions. *J. Geophys. Res.* **118**, 2140–2158 (2013).

35. C. F. Dow, F. S. McCormack, D. Young, J. S. Greenbaum, J. Roberts, D. Blankenship, Totten Glacier subglacial hydrology determined from geophysics and modeling. *Earth Planet. Sci. Lett.* **531**, 115961 (2020).

36. C. M. Little, A. Gnanadesikan, M. Oppenheimer, How ice shelf morphology controls basal melting. *J. Geophys. Res.* **114**, C12007 (2009).

37. C. Kittle, C. Amory, S. Hofer, C. Agosta, N. C. Jourdain, E. Gilbert, L. L. Toumelin, E. Vignon, H. Gallée, X. Fettweis, Clouds drive differences in future surface melt over the Antarctic Ice Sheet. *Cryosphere.* **16**, 2655–2669 (2021).

38. S. Ehrenfeucht, M. Morlighem, E. Rignot, C. F. Dow, J. Mouginot, Seasonal acceleration of Petermann Glacier, Greenland, from changes in subglacial hydrology. *Geophys. Res. Lett.* **50**, e2022GL098009 (2022).

39. C. Schoof, Ice sheet grounding line dynamics: Steady states, stability, and hysteresis. *Case Rep. Med.* **112**, F03S28 (2007).

40. R. M. DeConto, D. Pollard, Contribution of Antarctica to past and future sea-level rise. *Nature* **531**, 591–597 (2016).

41. R. M. DeConto, D. Pollard, R. B. Alley, I. Velicogna, E. Gasson, N. Gomez, S. Sadai, A. Condron, D. M. Gilford, E. L. Ashe, R. E. Kopp, D. Li, A. Dutton, The Paris Climate Agreement and future sea-level rise from Antarctica. *Nature* **593**, 83–89 (2021).

42. C. F. Dow, M. A. Werder, S. Nowicki, R. T. Walker, Modeling Antarctic subglacial lake filling and drainage cycles. *Cryosphere* **10**, 1381–1393 (2016).

43. C. F. Maule, M. E. Purucker, N. Olsen, K. Mosegaard, Heat flux anomalies in Antarctica revealed by satellite magnetic data. *Science* **309**, 464–467 (2005).

44. H. Seroussi, S. Nowicki, A. J. Payne, H. Goelzer, W. H. Lipscomb, A. Abe-Ouchi, C. Agosta, T. Albrecht, X. Asay-Davis, A. Barthel, R. Calov, R. Cullather, C. Dumas, B. K. Galton-Fenzi, R. Gladstone, N. R. Golledge, J. M. Gregory, R. Greve, T. Hattermann, M. J. Hoffman, A. Humbert, P. Huybrechts, N. C. Jourdain, T. Kleiner, E. Larour, G. R. Leguy, D. P. Lowry, C. M. Little, M. Morlighem, F. Pattyn, T. Pelle, S. F. Price, A. Shepherd, E. Simon, R. S. Smith, F. Straneo, S. Sun, L. D. Trusel, J. V. Breedam, R. S. W. van de Wal, R. Winkelmann, C. Zhao, T. Zhang, T. Zwinger, ISMIP6 Antarctica: A multi-model ensemble of the Antarctic ice sheet evolution over the 21st century. *Cryosphere* **14**, 3033–3070 (2020).

45. H. Seroussi, M. Morlighem, E. Larour, E. Rignot, A. Khazendar, Hydrostatic grounding line parameterization in ice sheet models. *Cryosphere* **8**, 2075–2087 (2014).

46. H. Seroussi, M. Morlighem, Representation of basal melting at the grounding line in ice flow models. *Cryosphere* **12**, 3085–3096 (2018).

47. D. R. MacAyeal, Large-scale ice flow over a viscous basal sediment: Theory and application to Ice Stream B, Antarctica. *J. Geophys. Res.* **94**, 4071–4087 (1989).

48. J. Mouginot, E. Rignot, B. Scheuchl, Continent-wide, interferometric SAR phase, mapping of Antarctic ice velocity. *Geophys. Res. Lett.* **46**, 9710–9718 (2019).

49. M. Morlighem, H. Seroussi, E. Larour, E. Rignot, Inversion of basal friction in Antarctica using exact and incomplete adjoints of a higher-order model. *J. Geophys. Res.* **118**, 1746–1753 (2013).

50. C. Schoof, The effect of cavitation on glacier sliding. *Proc. R. Soc. A.* **461**, 609–627 (2005).

51. I. Joughin, B. E. Smith, C. G. Schoof, Regularized Coulomb friction laws for ice sheet sliding: Application to Pine Island Glacier, Antarctica. *Geophys. Res. Lett.* **46**, 4764–4771 (2019).

52. K. M. Cuffey, W. S. B. Paterson, *The Physics of Glaciers* (Elsevier, ed. 4, 2010).

53. J. M. van Wessem, W. J. van de Berg, B. P. Y. Noël, E. van Meijgaard, C. Amory, G. Birnbaum, C. L. Jakobs, B. Krüger, K. T. M. Lenaerts, S. Lhermitte, S. R. M. Ligtenberg, B. Medley, C. H. Reijmer, K. van Tricht, L. D. Trusel, L. H. van Ulft, B. Wouters, J. Wuite, M. R. van den Broeke, Modelling the climate and surface mass balance of polar ice sheets using RACMO2 —Part 2: Antarctica (1979-2016). *Cryosphere* **12**, 1479–1498 (2018).

54. T. Pelle, M. Morlighem, Y. Nakayama, H. Seroussi, Widespread grounding line retreat of Totten Glacier, East Antarctica, over the 21st Century. *Geophys. Res. Lett.* **48**, e2021GL093213 (2021).

55. H. Zhang, D. Menemenlis, I. Denty, ECCO LLC270 ocean-ice state estimate (Tech. Rep., Jet Propulsion Laboratory, California Institute of Technology, 2018); http://hdl.handle.net/1721.1/119821.

56. D. Dee, S. M. Uppala, A. J. Simmons, P. Berrisford, P. Poli, S. Kobayashi, U. Andrae, M. A. Balmaseda, G. Balsamo, P. Bauer, P. Bechtold, A. M. C. Beljaars, L. van de Berg, J. Bidlot, N. Bormann, C. Delsol, R. Dragani, M. Fuentes, A. J. Geer, L. Haimberger, S. B. Healy, H. Hersbach, E. V. Hólm, L. Isaksen, P. Kållberg, M. Köhler, M. Matricardi, A. P. McNally, B. M. Monge-Sanz, J. Morcrette, B. K. Park, C. Peubey, P. de Rosnay, C. Tavolato, J. N. Thépaut, F. Vitart, The ERA-Interim reanalysis: Configuration and performance of the data assimilation system. *QJR Meteorol. Soc.* **137**, 553–597 (2011).

57. V. Eyring, S. Bony, G. A. Meehl, C. A. Senior, B. Stevens, R. J. Stouffer, K. E. Taylor, Overview of the Coupled Model Intercomparison Project Phase 6 (CMIP6) experimental design and organization. *Geosci. Model Dev.* **9**, 1937–1958 (2016).

58. T. Pelle, J. S. Greenbaum, C. F. Dow, A. Jenkins, M. Morlighem, Data from: Subglacial discharge accelerates future retreat of Denman and Scott Glaciers, East Antarctica. *Dryad Digital Repository* doi:10.7280/D1X12S (2023).